



Seismic attenuation beneath Europe and the North Atlantic: Implications for water in the mantle

Hejun Zhu ^{a,*}, Ebru Bozdağ ^a, Thomas S. Duffy ^a, Jeroen Tromp ^{a,b}

^a Department of Geosciences, Princeton University, Princeton, NJ, USA

^b Program in Applied & Computational Mathematics, Princeton University, Princeton, NJ, USA



ARTICLE INFO

Article history:

Received 17 June 2013

Received in revised form 12 August 2013

Accepted 13 August 2013

Available online 11 September 2013

Editor: P. Shearer

Keywords:

adjoint tomography

seismic attenuation

the mantle transition zone

subduction zones

water transport

ABSTRACT

It is well known that anelasticity has significant effects on the propagation of seismic waves, as manifested by physical dispersion and dissipation. Investigations of anelasticity provide complementary constraints on the physical properties of Earth materials, but – contrary to imaging with elastic waves – progress in mapping Earth's anelasticity has been relatively slow, and there is only limited agreement between different studies or methodologies. Here, within the framework of adjoint tomography, we use frequency-dependent phase and amplitude anomalies between observed and simulated seismograms to simultaneously constrain upper mantle wavespeeds and attenuation beneath the European continent and the North Atlantic Ocean. In the sea-floor spreading environment beneath the North Atlantic, we find enhanced attenuation in the asthenosphere and within the mantle transition zone (MTZ). In subduction zone settings, for example beneath the Hellenic arc, elevated attenuation is observed along the top of the subducting slab down to the MTZ. No prominent reductions in wavespeeds are correlated with these distinct attenuation features, suggesting that non-thermal effects may play an important role in these environments. A plausible explanation invokes the transport of water into the deep Earth by relatively cold subducting slabs, leading to a hydrated MTZ, as previously suggested by mineral physics and geodynamics studies.

© 2013 Elsevier B.V. All rights reserved.

1. Introduction

Current knowledge of heterogeneities in the Earth's mantle primarily comes from tomographic studies of elastic wavespeeds. Based on traveltimes of body waves, dispersion of surface waves, and splitting of free oscillations, seismologists routinely estimate lateral variations in elastic wavespeeds within the Earth's interior (e.g., Woodhouse and Dziewonski, 1984; Van der Hilst et al., 1997; Romanowicz, 2003; Montelli et al., 2004). However, Earth materials exhibit anelasticity, an energy dissipation mechanism that manifests itself in the form of physical dispersion and attenuation of seismic waves (Liu et al., 1976). 3D maps of lateral variations in anelastic attenuation provide complementary constraints on variations in temperature, water content, partial melt, and composition (Karato, 2003). For instance, guided by mineral physics experiments, Shito et al. (2006) combined tomographic images of elastic wavespeeds and anelastic attenuation to estimate 3D variations in temperature, water content and other parameters, such as major element chemistry and melt fraction.

There is no consensus among seismologists on how the effects of attenuation should be quantified and measured. Contrary

to wavespeed models, existing global models of attenuation exhibit limited agreement, e.g., Romanowicz (1995), Gung and Romanowicz (2004), Dalton et al. (2008). In contrast to body-wave traveltimes or surface-wave dispersion, which are solely governed by seismic wavespeeds, seismic wave amplitudes are affected by a host of competing factors besides anelastic attenuation, such as earthquake magnitudes and radiation patterns, elastic focusing and defocusing, and scattering (Ruan and Zhou, 2010, 2012).

We have developed a new tomographic technique, called “adjoint tomography” (Tromp et al., 2005; Tape et al., 2007, 2009, 2010; Liu and Tromp, 2008; Zhu et al., 2012), to simultaneously constrain elastic wavespeeds and anelastic attenuation. Frequency-dependent phase and amplitude differences between observed and simulated seismograms (Laske and Masters, 1996; Ekström et al., 1997; Zhou et al., 2004) are simultaneously considered in the inversion in order to ensure a consistent treatment between anelastic attenuation and elastic focusing/defocusing (Billien et al., 2000). Synthetic seismograms are computed based on a spectral-element method (Komatsch and Tromp, 1999; Peter et al., 2011), and Fréchet derivatives with respect to the model parameters are numerically calculated in a 3D background model based on adjoint methods (Lailly, 1983; Tarantola, 1984; Tromp et al., 2005; Liu and Tromp, 2008). Body and surface waves recorded in three-component seismograms are combined to simultaneously constrain

* Corresponding author.

E-mail address: hejunzhu@princeton.edu (H. Zhu).

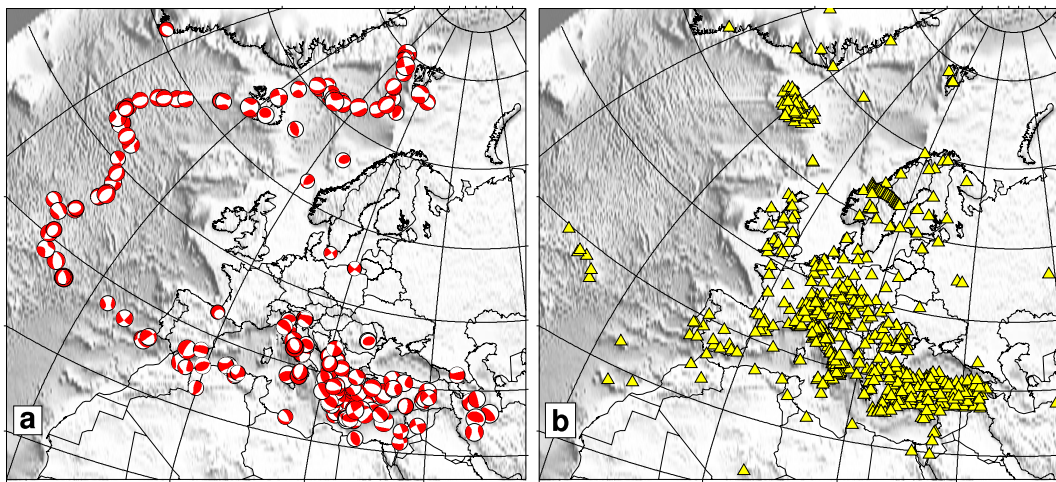


Fig. 1. Distribution of earthquakes and seismographic stations. a. Location of earthquakes used in the inversion. b. Location of stations.

deep and shallow upper mantle structures (Zhu et al., 2012). Based on a preconditioned conjugate gradient method (Fletcher and Reeves, 1964), we iteratively improve the elastic and anelastic models and gradually reduce the phase and amplitude differences.

2. Dataset and method

2.1. Dataset

In this study, 190 earthquakes recorded by 745 seismographic stations are used to illuminate the crust and upper mantle structure of the European continent and the North Atlantic Ocean (Zhu et al., 2012). Most earthquakes are shallow events with magnitudes ranging from 4.5 to 6.5 and occurring between 1996 and 2011. They are predominantly distributed along the northern Mid-Atlantic Ridge and the Mediterranean-Himalayan Belt. Observed seismograms are collected from the Incorporated Research Institutions for Seismology (IRIS, www.iris.edu), Observatories and Research Facilities for European Seismology (ORFEUS, www.orfeus-eu.org) and the Kandilli Observatory (www.koeri.boun.edu.tr). Additionally, seismic array data from several IRIS/PASSCAL experiments are incorporated in the inversion to constrain local structures, such as underneath Iceland and the Anatolian Plate. Fig. 1 shows the distribution of earthquakes and stations. We have very good data coverage for the upper mantle beneath the European continent and the North Atlantic Ocean. Epicentral distances for our dataset range from a few degrees to more than 60 degrees. A simplified tectonic map of the European continent is shown in Fig. 2, and will be used as a reference for tomographic features discussed in Section 3.

2.2. Starting model

A new 3D crust and upper mantle model of Europe and the North Atlantic Ocean, EU₃₀ (Zhu et al., 2012), is used as the starting elastic model. EU₃₀ was constructed based on adjoint tomography (Tape et al., 2009, 2010; Zhu et al., 2012). Three-component body and surface waves were combined to constrain radially anisotropic shear wavespeeds throughout the European upper mantle. Thirty preconditioned conjugate gradient iterations (Fletcher and Reeves, 1964) were performed to minimize frequency-dependent phase differences between observed and simulated seismograms, requiring more than 17 100 wavefield simulations and 2.3 million central processing unit core hours. Fig. 3c and d illustrate relative perturbations in vertically and horizontally

polarized shear wavespeeds in EU₃₀ at a depth of 75 km. In addition, the 1D (radial) shear quality factor Q_μ profile from reference model STW105 (Kustowski et al., 2008a) is chosen as the starting anelastic model (Fig. 3b). Since the bulk quality factor Q_κ is much larger than the shear quality factor Q_μ (Durek and Ekström, 1996), only shear attenuation is considered in this paper. For brevity, in the rest of this paper, we use the symbol Q , rather than Q_μ , to denote the shear quality factor.

2.3. Misfit functions

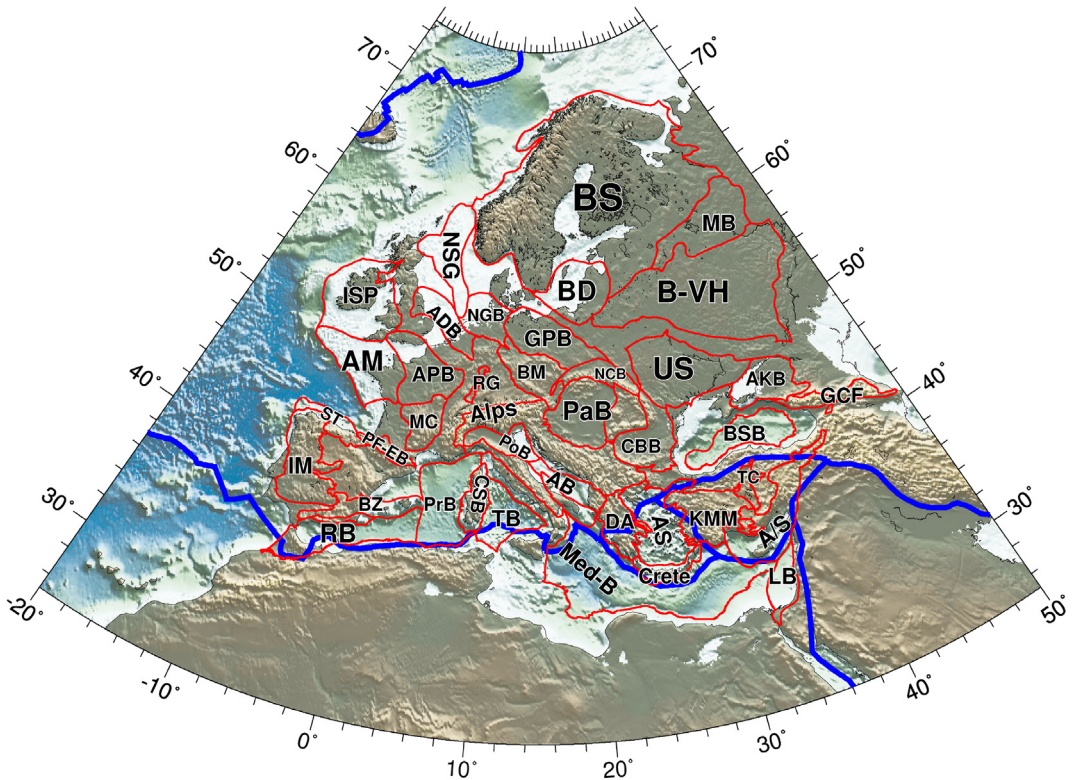
Phase and amplitude differences between data and synthetics are combined to simultaneously constrain elastic and anelastic structures. Therefore, the total misfit function χ is expressed as

$$\chi = w_\phi \chi^\phi + w_A \chi^A, \quad (1)$$

where χ^ϕ and χ^A are phase and amplitude contributions to the misfit, and w_ϕ and w_A denote corresponding weighting factors, which are used to balance relative contributions of phase and amplitude.

Three-component body and surface waves are combined to simultaneously constrain deep and shallow structures. Therefore, both phase and amplitude misfits in Eq. (1) involve six categories: P-SV body waves on vertical and radial components, SH body waves on transverse components; Rayleigh surface waves on vertical and radial components and Love surface waves on transverse components. For the first iteration, 15–40 s body waves and 40–100 s surface waves are used. As the models and the corresponding synthetic seismograms improve, the corner period of the surface wave measurements is gradually reduced from 40 s to 25 s (for details see Section 2.6).

FLEXWIN (Maggi et al., 2009), an automatic window selection tool, is used to select windows in the data suitable for making phase and amplitude measurements. These windows are selected based on similarities between observed and simulated seismograms. Unlike in classical traveltome tomography, no specific phases, such as P or S, are targeted: any window in which the observed and simulated seismograms are sufficiently close is suitable. A multitaper approach (Laske and Masters, 1996; Ekström et al., 1997; Zhou et al., 2004) is used to quantify frequency-dependent phase and amplitude discrepancies between observed and simulated seismograms in the windows selected by FLEXWIN. In this approach, the phase and amplitude misfits in Eq. (1) may be expressed as



AB: Adriatic Basin	BS: Baltic Shield	KMM: Kardiff/Menders Massif	PoB: Po Basin
ADB: Anglo-Dutch Basin	B-VH: Belorussian-Voronezh High	LB: Levantine Basin	PrB: Provence Basin
AKB: Azov-Kuban Basin	BZ: Betic Zone	MC: Massif Central	RB: Rif Basin
AM: Armorican Massif	CBB: Carpathian-Balkanian Basin	Med-B: Mediterranean Basin	RG: Rhine Graben
APB: Anglo-Paris Basin	CSB: Corsican-Sardinian Basin	MB: Moscow Basin	ST: Spanish Trough
AS: Aegean Sea	DA: Dinaric Alps	NCB: North Carpathian Basin	TB: Tyrrhenian Basin
A/S: Adana/Sivas	GCF: Great Caucasus Foldbelt	NGB: Northwest German Basin	TC: Tuz/Corum
BD: Baltic Depression	GPB: German-Polish Basin	NSG: North Sea Graben	US: Ukrainian Shield
BM: Bohemia Massif	IM: Iberian Massif	PaB: Pannonian Basin	
BSB: Black Sea Basin	ISP: Ireland-Scotland Platform	PF-EB: Pyrenean Foothills-Ebro Basin	

Fig. 2. Main tectonic structures of the European continent. Blue lines denote plate boundaries (Bird, 2003). (For interpretation of the references to color in this figure caption, the reader is referred to the web version of this article.)

$$\chi^\phi = \sum_{c=1}^{N_c} w_c \sum_{m=1}^{N_m} \int w_m \left[\frac{\Delta \tau_m(\omega)}{\sigma_m^\phi(\omega)} \right]^2 d\omega, \quad (2)$$

$$\chi^A = \sum_{c=1}^{N_c} w_c \sum_{m=1}^{N_m} \int w_m \left[\frac{\Delta \ln A_m(\omega)}{\sigma_m^A(\omega)} \right]^2 d\omega, \quad (3)$$

respectively, where N_c denotes the number of categories (i.e., $N_c = 6$ in this study), w_c is a weighting factor for each category equaling the reciprocal of the number of measurements in each category, N_m (i.e., $w_c = 1/N_m$), w_m represents weighting factors associated with the multitaper measurements, $\Delta \tau_m(\omega)$ and $\Delta \ln A_m(\omega)$ are frequency-dependent phase and amplitude anomalies, and $\sigma_m^\phi(\omega)$ and $\sigma_m^A(\omega)$ denote uncertainties associated with these measurements.

2.4. Model parameters

Model parameters in this study include the wavespeeds of horizontally traveling and vertically or horizontally polarized shear

waves, β_v and β_h , respectively, the bulk sound wavespeed c , the dimensionless radially anisotropic parameter η , and the inverse shear quality factor Q^{-1} . Mass density, ρ , has less of an effect on seismic measurements than wavespeeds and shear attenuation. An empirical relationship between relative perturbations in mass density and isotropic shear wavespeed is used to update the density structure (Montagner and Anderson, 1989), namely

$$\delta \ln \rho = 0.33 \delta \ln \beta, \quad (4)$$

where β denotes the Voigt average of the radially anisotropic shear wavespeeds (Babuška and Cara, 1991)

$$\beta = \sqrt{\frac{2\beta_v^2 + \beta_h^2}{3}}. \quad (5)$$

Based on the definition of the total misfit function in Eq. (1) and the model parameterization discussed above, we are able to express perturbations in total misfit as

$$\delta \chi = \int_V K_{\beta_v} \delta \ln \beta_v + K_{\beta_h} \delta \ln \beta_h + K_c \delta \ln c + K_\eta \delta \ln \eta$$

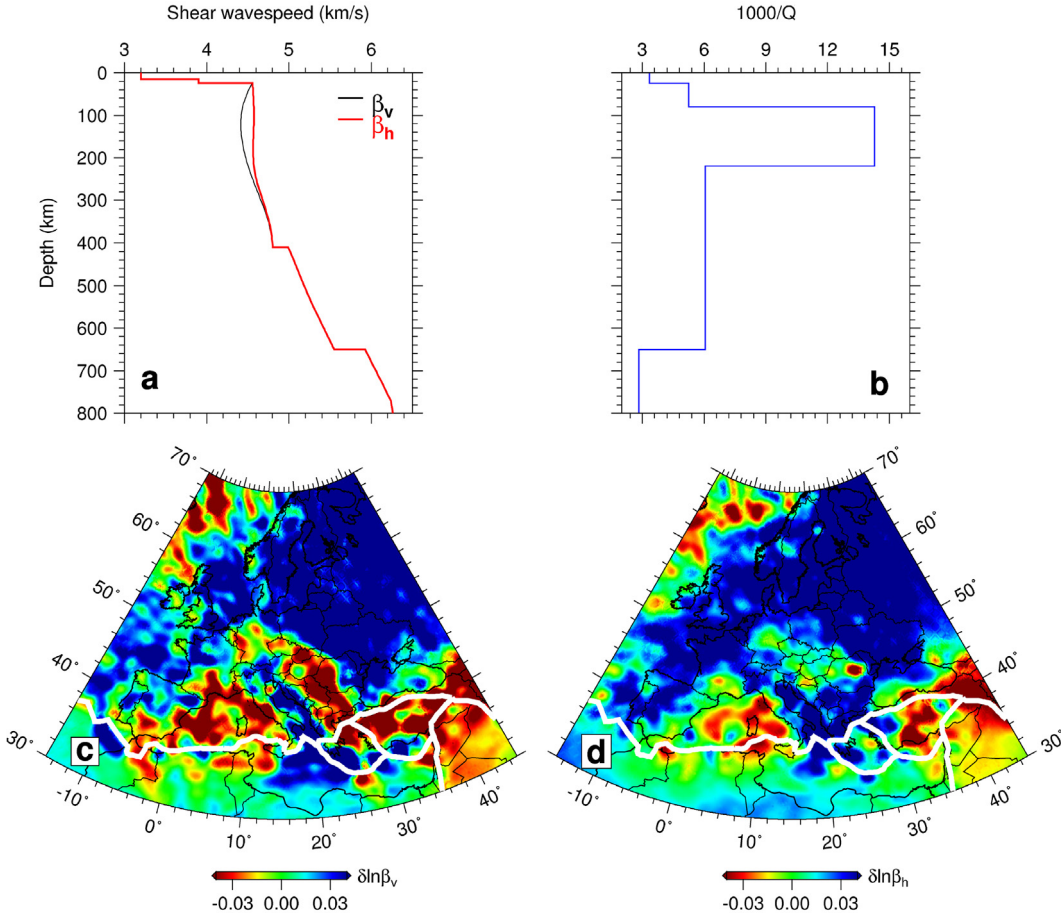


Fig. 3. Elastic and anelastic structure of starting model EU₃₀. a. 1D shear wavespeed profiles of STW105 (Kustowski et al., 2008a). Black and red lines denote vertically (β_v) and horizontally (β_h) polarized shear wavespeeds, respectively, which are used as a reference model to compute relative perturbations in c and d. b. 1D shear Q profile of STW105. c. Relative perturbations in vertically polarized shear wavespeed β_v in starting model EU₃₀ at 75 km depth. d. Relative perturbations in horizontally polarized shear wavespeed β_h in EU₃₀ at 75 km depth. White lines in c and d denote plate boundaries (Bird, 2003).

$$+ K_{Q^{-1}} \delta Q^{-1} dV, \quad (6)$$

where V refers to the Earth's volume, and K_{β_v} , K_{β_h} , K_c , K_η , and $K_{Q^{-1}}$ are 3D Fréchet derivatives with respect to the five model parameters β_v , β_h , c , η , and Q^{-1} . Dimensionless logarithmic perturbations are used for the four elastic model parameters β_v , β_h , c , and η , but we choose to use the inverse shear quality factor Q^{-1} to represent perturbations in shear attenuation in order to balance the magnitudes of the Fréchet derivatives. With this parameterization, all model parameters are dimensionless and of comparable size. The smallest absolute Q value is limited to 50, but a more typical value on the low end is 70–100.

Based on the results of Tromp et al. (2005), the Fréchet derivative with respect to shear attenuation may be expressed as

$$K_{Q^{-1}} = - \int_0^T 2\mu(\mathbf{x}) \mathbf{D}^\dagger(\mathbf{x}, T-t) : \mathbf{D}(\mathbf{x}, t) dt, \quad (7)$$

where \mathbf{D} and \mathbf{D}^\dagger are forward and adjoint traceless strain deviators. The adjoint source that is used to generate the adjoint strain deviator \mathbf{D}^\dagger in Eq. (7) is

$$\begin{aligned} \tilde{f}_i^\dagger(\mathbf{x}, t) &= \frac{1}{2\pi} \int_{-\infty}^{+\infty} [(2/\pi) \ln(|\omega|/\omega_0) - i \operatorname{sgn}(\omega)]^* \\ &\times f_i^\dagger(\mathbf{x}, \omega) \exp(i\omega t) d\omega, \end{aligned} \quad (8)$$

where $f_i^\dagger(\mathbf{x}, \omega)$ is the adjoint source used to compute Fréchet derivatives with respect to the four elastic model parameters β_v , β_h , c , and η . Therefore, in order to simultaneously determine Fréchet derivatives with respect to elastic wavespeeds and shear attenuation, two separate adjoint simulations are required for each earthquake at each iteration: one utilizing the regular adjoint source f_i^\dagger for the elastic model parameters, and a second driven by the adjoint source \tilde{f}_i^\dagger for shear attenuation.

2.5. Source correction

Origin times, t_0 , and scalar moments, M_0 , of earthquakes have a direct impact on phases and amplitudes of simulated seismograms. Therefore, in this study, several iterations of source corrections are performed during the structural inversion in order to reduce biases due to source parameter uncertainties. A simple 2D grid search is used to correct the origin time and scalar moment of each earthquake. First, the simulated seismograms are corrected by a pair of perturbations in origin time and scalar moment (Δt_0 , $\Delta \ln M_0$) within a certain range, for instance $-5 \text{ s} < \Delta t_0 < 5 \text{ s}$ and $-0.8 < \Delta \ln M_0 < 0.8$. Next, cross-correlation measurements are used to calculate phase and amplitude differences between observed seismograms, $\mathbf{d}(\mathbf{x}, t)$, and corrected synthetic seismograms, $(1 + \Delta \ln M_0)\mathbf{s}(\mathbf{x}, t + \Delta t_0)$. The misfit function is defined as a weighted combination of phase and amplitude differences as in Eq. (1). Finally, a grid search is used to find the pair (Δt_0 , $\Delta \ln M_0$) that minimizes the misfit.

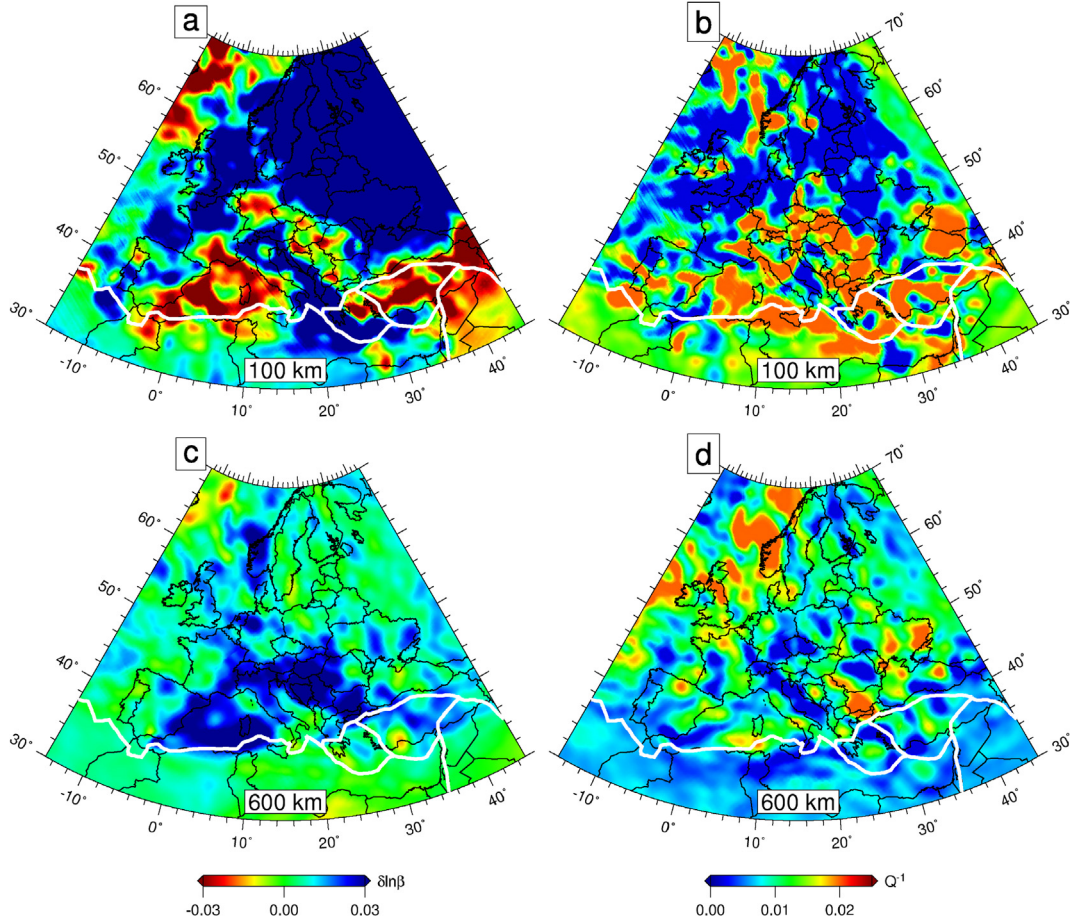


Fig. 4. Horizontal cross sections of isotropic shear wavespeed (left column) and shear attenuation (right column) for model EU₅₀. a and c. Relative perturbations in isotropic shear wavespeed at depths of 100 km and 600 km, respectively. b and d. Shear attenuation at depths of 100 km and 600 km, respectively. White lines indicate plate boundaries (Bird, 2003).

Figs. S1 and S2 (see the supplementary material) illustrate the improvements in amplitude and phase fits after the source corrections. The average values of the measurements are improved in all six categories while the standard deviations remain almost the same. This illustrates that source corrections improve the mean phase and amplitude anomalies, but that a 3D attenuation model is required to reduce the standard deviations.

2.6. Improvements in misfits and histograms

Twenty preconditioned conjugate gradient iterations are performed to obtain a new crust and upper mantle model, named EU₅₀, which required more than 18 050 wavefield simulations and 2.5 million central processing unit core hours. Both phase and amplitude misfits are significantly reduced after these iterations. In Fig. S3 (see the supplementary material), the overall amplitude misfit as well as the contributions from the six body- and surface-wave categories are gradually reduced. In the structural inversion, we start with long-period measurements for surface waves, and short-period information is gradually incorporated, e.g., the short-period corner for surface waves is gradually reduced from 40 s to 25 s. This strategy allows us to first resolve large-scale features. With gradual improvements in models and simulated seismograms, shorter-period measurements are included to constrain smaller-scale features. Meanwhile, phase misfits are also gradually reduced during the iterations (see Fig. S4 in the supplementary material).

Fig. S5 in the supplementary material compares histograms of amplitude anomalies for the starting model (after the source cor-

rection) and the new model, EU₅₀. Both the average values and standard deviations of amplitude anomalies are considerably reduced in all six categories. As shown in Fig. S6 in the supplementary material, the phase anomalies of the new model are also significantly reduced compared with the starting model.

2.7. Comparisons with previous models

To help validate our joint inversion strategy for body and surface waves, we compare wavespeed model EU₅₀ with previous surface- and body-wave models. In Fig. S7 of the supplementary material we compare the isotropic shear wavespeed of EU₅₀ at a depth of 100 km with five surface-wave models, namely, EP-mantle (Schivardi and Morelli, 2011), Chang2010 (Chang et al., 2010), S2.9EA (Kustowski et al., 2008b), LRSP30EU02 (Boschi et al., 2009) and CUSDT (Shapiro and Ritzwoller, 2002). Model EU₅₀ correlates well with these five models at this shallow depth. In Fig. S8 of the supplementary material we compare the isotropic shear wavespeed of EU₅₀ with compressional wavespeed model LLNL-G3Dv3 (Simmons et al., 2012) at depths of 80 km and 600 km. There is good agreement between our model and this body-wave model at these depths.

3. Tomographic images and discussion

3.1. Horizontal cross sections

Fig. 4 presents horizontal cross sections of isotropic shear wavespeed (β) and shear attenuation (Q^{-1}) in model EU₅₀ at

depths of 100 km and 600 km. Relative perturbations in shear wavespeed are calculated with respect to 1D reference model STW105 (Fig. 3a). At 100 km depth, the isotropic shear wavespeed image contains numerous interesting features correlated with well-known tectonic provinces (Figs. 4a and 2). For instance, we observe a sharp contrast associated with the Tornquist–Teisseyre Suture Zone, separating the Precambrian East European Platform from Phanerozoic central and eastern Europe. The Tyrrhenian Sea and the Anatolian Plate are revealed as two prominent slower-than-average wavespeed anomalies. In central and eastern Europe, there are several notable slow wavespeed anomalies associated with the Massif Central, the Rhine Graben, the Eifel Hotspot, the Bohemian Massif as well as the Pannonian Basin. At this shallow depth, most regions show an interesting relation between shear wavespeed and attenuation (Fig. 4b). For example, the East European Platform is characterized by fast shear wavespeed and low attenuation while the Tyrrhenian Sea is characterized by slow shear wavespeed and high attenuation. These features suggest that the same factors, e.g., temperature, control both elastic wavespeeds and anelastic attenuation at shallow depths (Billien et al., 2000; Dalton et al., 2008). In addition, some areas, e.g., the Anatolian Plate, involve more complicated relations between shear wavespeed and attenuation.

At a depth of 600 km, central and eastern Europe are dominated by two prominent faster-than-average wavespeed anomalies (Fig. 4c). These features might be related to remnants of slab roll-back due to trench migration over the past 30 million years, a process responsible for the current Apennines–Calabrian–Maghrebides, Carpathian–Vrancea, and Hellenic–Cyprus arcs (Wortel and Spakman, 2000). Our isotropic shear wavespeed images are consistent with previous traveltimes-based body-wave tomographic studies (Wortel and Spakman, 2000; Piromallo and Morelli, 2003). However, as illustrated in Fig. 4d, there are no strong lower-than-average attenuation anomalies which correspond to slab remnants at a depth of 600 km, indicating that different factors control elastic wavespeeds and anelastic attenuation at greater depths. Previous global-scale attenuation studies also demonstrated that correlations between attenuation and shear wavespeed decrease significantly below depths of 200–250 km (Billien et al., 2000; Gung and Romanowicz, 2004; Dalton et al., 2008).

3.2. MTZ beneath the North Atlantic Ocean

Model EU₅₀ contains several notable features in shear attenuation beneath the North Atlantic Ocean. A number of vertical cross sections perpendicular to the northern Mid-Atlantic Ridge are used to illustrate these features in Fig. 5. At shallow depths, the oceanic and continental lithosphere are characterized by low attenuation, e.g., in N3, N4, and N5. At depths ranging from 80 km to 200 km, we observe a prominent enhanced attenuation layer associated with the oceanic asthenosphere. The most striking feature of shear attenuation in these vertical cross sections is enhanced attenuation within the MTZ beneath the North Atlantic Ocean, for instance in cross sections N2 and N4. Interestingly, there are no strong reductions in shear wavespeed related to the highly attenuating MTZ (see Fig. S9 in the supplementary material), suggesting that non-thermal effects, such as water content, grain size, or compositional variations, may play important roles in this environment.

There is growing evidence for enhanced water content in the transition zone. The major minerals of this region, wadsleyite and ringwoodite, have water solubilities that are an order of magnitude larger than for minerals in the shallow upper mantle (Kohlstedt et al., 1996). Electrical conductivity measurements are consistent with higher water content in the transition zone compared to the

rest of the upper mantle (Karato, 2011). The transition zone water filter hypothesis was proposed to explain discrepancies between geophysical and geochemical observations (Bercovic and Karato, 2003). A thin melt layer on top of the 410 km discontinuity, an important prediction of this hypothesis, was found beneath the western United States by both seismological and electromagnetic studies (Song et al., 2004; Coutier and Revenaugh, 2007; Tauzin et al., 2010), indicating that a hydrated MTZ might exist, at least on regional scales.

The presence of small quantities of water (~ 0.1 wt%) is expected to have a modest effect on seismic wavespeeds but may have a strong effect on attenuation (Shito et al., 2006; Karato, 2011). Thus, elevated attenuation in the absence of marked reductions in shear wavespeeds in the vertical cross sections shown in Fig. 5 might be indicative of a water-enriched MTZ beneath the North Atlantic Ocean. Furthermore, a hydrous MTZ has direct impact on the character of upper mantle discontinuities (Meijde et al., 2003). A receiver function study in the northern North Sea observed a significant weakening of the 660 km discontinuity (Helffrich et al., 2003), which was interpreted to be a consequence of a hydrated MTZ beneath the North Atlantic Ocean, an interpretation that is consistent with our images. Using body waveforms, Fuji et al. (2010) found a low shear quality factor within the MTZ beneath the Northwestern Pacific, reminiscent of our vertical cross sections beneath the North Atlantic Ocean. Interestingly, 1D radial Q model QL10 (Durek and Ekström, 1996) shows a slightly reduced shear quality factor in the transition zone, whereas the more coarsely parameterized 1D model QL6 (Durek and Ekström, 1996) does not. We speculate that the water-enriched MTZ beneath the North Atlantic Ocean might be due to ancient subduction related to the closure of the Iapetus Ocean during the Caledonian Orogeny. This interpretation, involving water transport during subduction, is corroborated by our wavespeeds and attenuation images of present-day subduction in the Hellenic and Apennines–Maghrebides arcs, as we discuss next.

3.3. Subduction zones

Over the past several decades, relationships between subducting slabs and Earth's deep water cycle have been investigated based on observations from seismology, mineral physics, and geodynamics (Karato, 2003; Jacobsen and van der Lee, 2006; Maruyama and Okamoto, 2007; Iwamori, 2007; Zhao et al., 2009). However, questions related to how much and how deep subducting slabs can transport water down into the mantle remain largely unresolved (Karato, 2003). Here, we examine relationships between isotropic shear wavespeeds, compressional-to-shear wavespeed ratios (V_P/V_S), and attenuation based on model EU₅₀ for two subduction zones in central and eastern Europe: the Hellenic and Apennines–Maghrebides arcs (Fig. 6). As illustrated in Figs. 6a, b, d and e, these subducting slabs are characterized by strong fast shear wavespeeds and low V_P/V_S ratios. The Hellenic slab penetrates the 660 km discontinuity down into the lower mantle while slabs associated with the Apennines–Maghrebides arc are stagnant within the MTZ, in agreement with previous teleseismic body-wave studies (Wortel and Spakman, 2000; Piromallo and Morelli, 2003). At depths shallower than 150–200 km, we observe reductions in shear wavespeed and elevated V_P/V_S ratios overlying the subducting plate. These anomalies might be related to partial melt associated with dehydration of subducting oceanic lithosphere and serpentinization of the mantle wedge (Bostock et al., 2002; Zhang et al., 2004; Maruyama and Okamoto, 2007; Iwamori, 2007).

Several attenuation studies have been used to investigate anelastic structure in subduction zones, e.g., Stachnik et al. (2004), Wiens et al. (2008), Rychert et al. (2008). In Figs. 6c and f, we

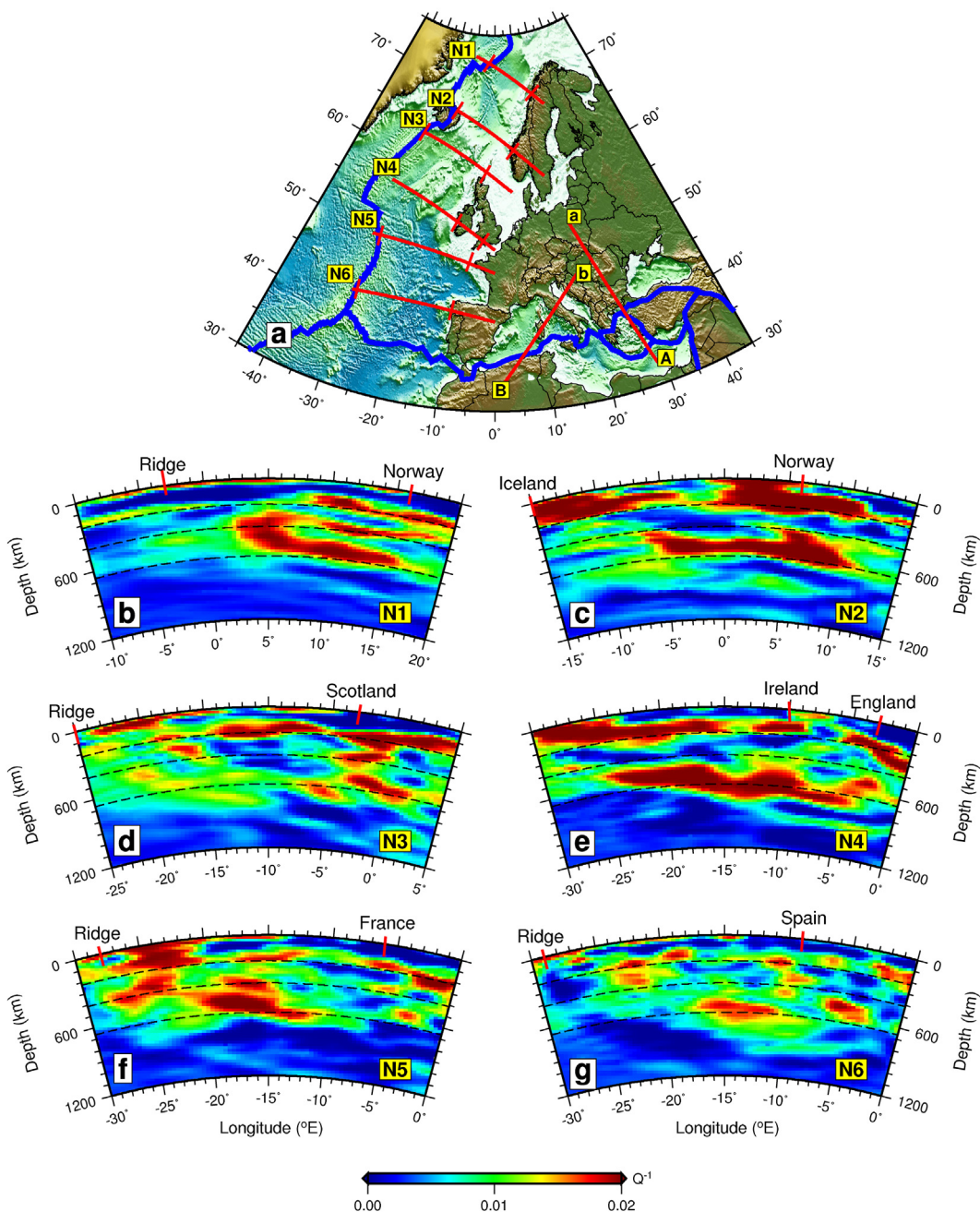


Fig. 5. Vertical cross sections of shear attenuation beneath the North Atlantic. a. Locations of vertical cross sections in b–g and Fig. 6. b–g. Shear attenuation for vertical cross sections N1–N6, perpendicular to the northern Mid-Atlantic Ridge. The dashed black lines in b–g denote the 220 km, 410 km and 660 km discontinuities.

observe channels of enhanced attenuation along the top of the seismically fast slabs down to the MTZ beneath the Hellenic and Apennines–Maghrebides arcs. Similar to the highly attenuating MTZ beneath the North Atlantic Ocean, there are no obvious corresponding reductions in shear wavespeed (Figs. 6a and d). Petrological and geodynamical models show that a significant amount of water can be carried down into the deep upper mantle by slabs if their thermal gradients are low or subduction speeds fast (Maruyama and Okamoto, 2007; Iwamori, 2007). Minerals such as lawsonite, phengite, and phase A or E may be responsible for transport of water in the slab into the MTZ (Maruyama and Okamoto, 2007), where it can be incorporated into nominally anhydrous phases such as wadsleyite and ringwoodite. This high-attenuation channel overlying the subducting slab might be a

complementary seismic indicator for the presence of highly water-soluble minerals in descending slabs.

Within the MTZ beneath these regions of subduction, portions of the slab are characterized by higher-than-average attenuation (Figs. 6c and f). Previous attenuation studies of subduction zones beneath Japan and south America demonstrated that shear Q -values of slabs within the MTZ might be as low as values within the asthenosphere (Sacks and Okada, 1974). Furthermore, global attenuation tomography, constrained by Rayleigh-wave phase and amplitude anomalies, has identified anomalies with high attenuation surrounding the Pacific. These high-attenuation features correlate with the locations of subducting slabs at MTZ depths (Billien et al., 2000). One plausible explanation for these higher-than-average attenuation anomalies is the presence of water transported

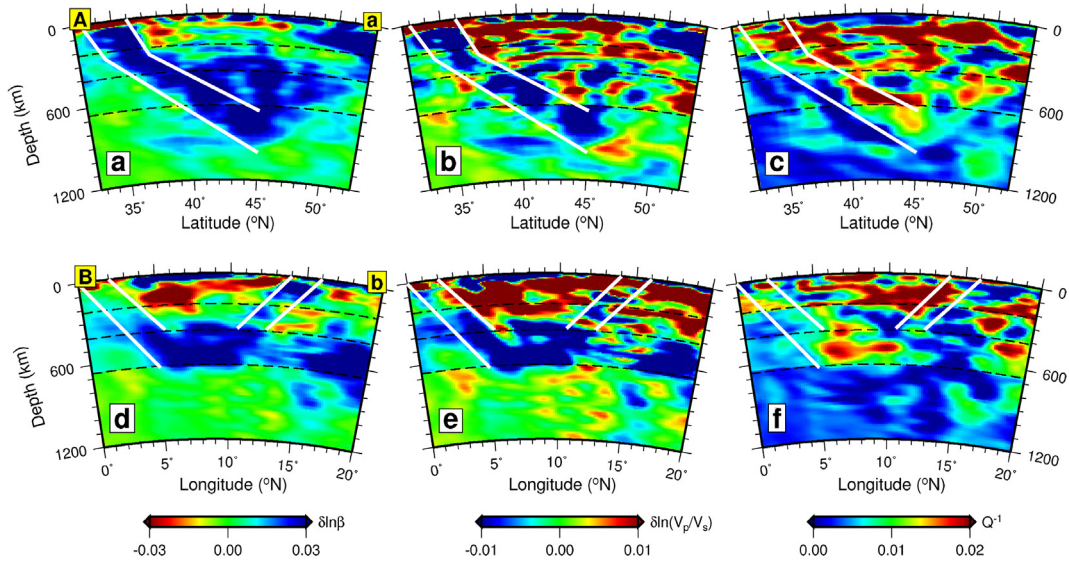


Fig. 6. Vertical cross sections of the Hellenic arc (top row) and the Apennines–Maghrebides arc (bottom row). a–c. Relative perturbations in isotropic shear wavespeed $\delta \ln \beta$, V_p/V_s ratio, and shear attenuation (Q^{-1}) of the Hellenic subduction zone. The location of cross section A–a is shown in Fig. 5a. d–f. Structures of the Apennines–Maghrebides subduction zone. The location of cross section B–b is shown in Fig. 5a. White lines outline the seismically fast subducting slabs.

down into the MTZ by subducting slabs. Such a scenario is consistent with speculation for a water-enriched MTZ beneath the Mediterranean region based on a receiver function study (Meijde et al., 2003). Enhanced attenuation extending into the top of the lower mantle (Fig. 6c) may reflect water (up to 0.1 wt%) carried into this region and incorporated in silicate perovskite (Lawrence and Wyession, 2006; Hernandez et al., 2013).

Electrical conductivity studies provide independent constraints on the amount and distribution of water within the deep mantle, because of its high sensitivity to the presence of hydrogen (Huang et al., 2005). A global 3D electromagnetic study has shown that high conductivity correlates well with cold subducting slabs around the circum-Pacific margin within the MTZ (Kelbert et al., 2009). Furthermore, an enhanced conductivity layer was imaged along the top of the subducting Nazca slab down to depths in excess of 250 km (Booker et al., 2004). These electromagnetic anomalies were attributed to the presence of water or water-induced partial melt within the deep Earth, in agreement with our interpretation of enhanced shear attenuation overlying subducting slabs as well as within the MTZ beneath the North Atlantic.

3.4. Resolution tests

The “approximate Hessian”, \tilde{H} , is a good proxy for ray density and resolution. It is calculated based on the expression

$$\tilde{H}(\mathbf{x}) = \int_0^T \partial_t^2 \mathbf{s}(\mathbf{x}, t) \cdot \partial_t^2 \mathbf{s}^\dagger(\mathbf{x}, T-t) dt, \quad (9)$$

where \mathbf{s} and \mathbf{s}^\dagger denote forward and adjoint wavefields, respectively. Fig. 7 illustrates the approximate Hessian in vertical cross sections perpendicular to the northern Mid-Atlantic Ridge. We have good ray coverage in these vertical cross sections, as discussed in Section 3.2.

The “point spread function” is used to assess image quality in the final model (Fichtner and Trampert, 2011, 2012). It may be calculated based on the expression

$$H \cdot \delta m \approx K(m + \delta m) - K(m), \quad (10)$$

where H denotes the Hessian and δm is a localized model perturbation with respect to the final model m . The Fréchet derivative K is calculated for both models m and $m + \delta m$. This is used to assess the curvature of the misfit function at a particular “point” in the model space, and reflects the degree of “blurring” of that point, thus, the nomenclature “point spread function”.

A spherical Gaussian function in shear attenuation is used to perturb model EU₅₀ beneath eastern Europe (Fig. 8) and the North Atlantic (Fig. S10 in the supplementary material). By comparing the resulting images for β_v , β_h and Q^{-1} , we conclude that there is weak tradeoff between elastic wavespeeds and anelastic attenuation. However, the test beneath eastern Europe (Fig. 8) demonstrates that we cannot resolve whether or not regions of high attenuation are partially located inside the Hellenic slab or entirely outside of it. In Fig. S11 of the supplementary material, we calculate the “point spread function” by perturbing β_v for model EU₅₀; again we see good resolution and limited tradeoff with anelasticity. We conclude that elastic and anelastic structures in the MTZ beneath eastern Europe and the North Atlantic are reasonably well resolved.

4. Conclusions

We use adjoint tomography to construct an anelastic upper mantle model of the European continent and the North Atlantic, named EU₅₀. Frequency-dependent phase and amplitude measurements are combined to simultaneously determine elastic wavespeeds and anelastic attenuation. Short-period body waves (15–40 s) and long-period surface waves (25–100 s) recorded in three-component seismograms are utilized to constrain deep and shallow upper mantle structures. Twenty preconditioned conjugate gradient iterations are performed, requiring 18 050 wavefields simulations and 2.5 million central processing unit core hours. Both phase and amplitude differences between observed and simulated seismograms are significantly reduced after these iterations. Resolution analyses show limited smearing in the tomographic images and weak tradeoffs between elastic and anelastic model parameters.

We find that regions with fast shear wavespeed anomalies correspond to regions with low attenuation at shallow depths, e.g., 100 km. However, at greater depths, this correspondence vanishes.

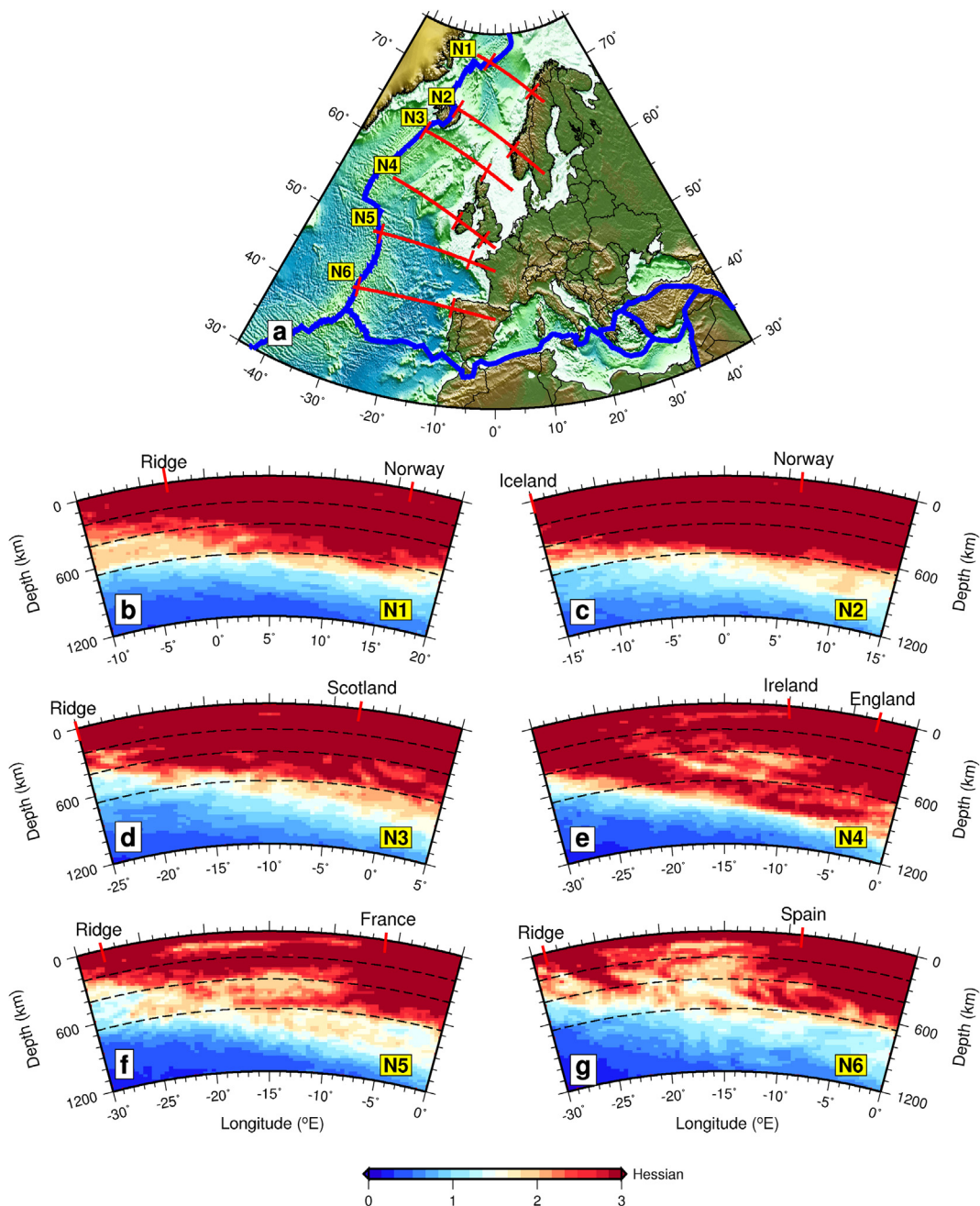


Fig. 7. Images of the approximate Hessian in vertical cross sections perpendicular to the northern Mid-Atlantic Ridge (see Fig. 5).

Enhanced attenuation anomalies are found within the asthenosphere and the MTZ beneath the North Atlantic Ocean, as well as along the top of the subducting slabs down to the MTZ beneath the Hellenic arc. There are no strong shear wavespeed reductions associated with these high-attenuation anomalies, suggesting a non-thermal origin. A plausible interpretation invokes the transport of water into the deep Earth by cold subducting slabs, leading to a water-enriched MTZ, in agreement with a previous hypothesis proposed based on mineral physics and geodynamics investigations.

Acknowledgements

This research was supported by the NSF under grants 1063057 and 1112906. We thank Shun-ichiro Karato and an anonymous re-

viewer for constructive reviews which helped to improve an earlier version of the manuscript. Numerical simulations were performed on a Dell cluster built and maintained by the Princeton Institute for Computational Science and Engineering (PICSciE). The open source spectral-element software package SPECFEM3D_GLOBE and the seismic measurement software package FLEXTWIN used in this study are freely available for download via the Computational Infrastructure for Geodynamics (CIG; geodynamics.org).

Appendix A. Supplementary material

Supplementary material related to this article can be found online at <http://dx.doi.org/10.1016/j.epsl.2013.08.030>.

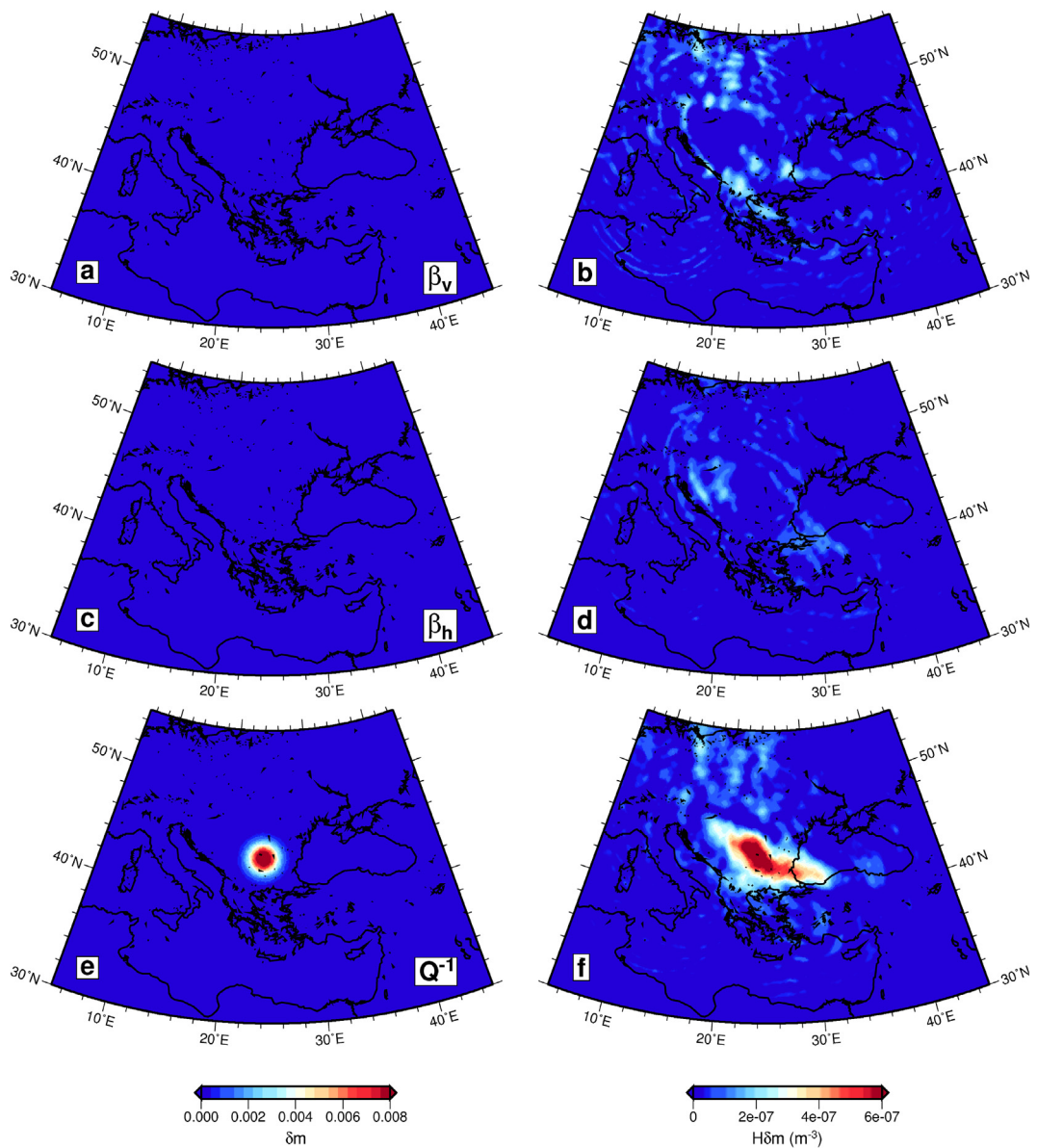


Fig. 8. Resolution analysis beneath Eastern Europe. a, c and e are horizontal cross section of model perturbation in β_v , β_h and Q^{-1} with respect to the final model EU₅₀ at 480 km depth. b, d and f are corresponding "point spread function" for β_v , β_h and Q^{-1} . The half width of Gaussian perturbation is 120 km.

References

- Babuska, V., Cara, M., 1991. Seismic Anisotropy in the Earth. Kluwer Academic Press, Boston, Massachusetts.
- Bercovici, D., Karato, S., 2003. Whole-mantle convection and the transition-zone water filter. *Nature* 425, 39–44.
- Billien, M., Leveque, J., Trampert, J., 2000. Global maps of Rayleigh wave attenuation for periods between 40 and 150 seconds. *Geophys. Res. Lett.* 27, 3619–3622.
- Bird, P., 2003. An update digital model of plate boundaries. *Geochem. Geophys. Geosyst.* 4 (3), 1027, <http://dx.doi.org/10.1029/2001GC000252>.
- Booker, J., Favetto, A., Poposilio, M., 2004. Low electrical resistivity associated with plunging of the Nazca flat slab beneath Argentina. *Nature* 429, 399–403.
- Boschi, L., Fry, B., Ekström, G., Giardini, D., 2009. The European upper mantle as seen by surface waves. *Surv. Geophys.* 30, 463–501.
- Bostock, M., Hyndman, R., Rondenay, S., Peacock, S., 2002. An inverted continental Moho and serpentinization of the forearc mantle. *Nature* 417, 536–538.
- Chang, S.J., der Lee, S.V., Flanagan, M., Bedle, H., Marone, F., Matzel, E., Pasayano, M., Rodgers, A., Romanowicz, B., Schmid, S., 2010. Joint inversion for three-dimensional S velocity mantle structure along the Tethyan margin. *J. Geophys. Res.* 115, B08309.
- Coutier, A., Revenaugh, J., 2007. Deep upper-mantle melting beneath the Tasman and Coral Seas detected with multiple ScS reverberations. *Earth Planet. Sci. Lett.* 259, 66–76.
- Dalton, C., Ekström, G., Dziewoński, A., 2008. The global attenuation structure of the upper mantle. *J. Geophys. Res.* 113, B09303, <http://dx.doi.org/10.1029/2007JB005429>.
- Durek, J., Ekström, G., 1996. A radial model of anelasticity consistent with long-period surface-wave attenuation. *Bull. Seismol. Soc. Am.* 86, 144–158.
- Ekström, G., Tromp, J., Larson, E., 1997. Measurement and global models of surface wave propagation. *J. Geophys. Res.* 102 (B4), 8137–8157.
- Fichtner, A., Trampert, J., 2011. Hessian kernels of seismic data functionals based upon adjoint techniques. *Geophys. J. Int.* 185, 775–798.
- Fichtner, A., Trampert, J., 2012. Resolution analysis in full waveform inversion. *Geophys. J. Int.* 187, 1604–1624.
- Fletcher, R., Reeves, C., 1964. Function minimization by conjugate gradients. *Comput. J.* 7, 149–154.
- Fuji, N., Kawai, K., Geller, R., 2010. A methodology for inversion of broadband seismic waveforms for elastic and anelastic structure and its application to the mantle transition zone beneath the Northwestern Pacific. *Phys. Earth Planet. Inter.* 180, 118–137.
- Gung, Y., Romanowicz, B., 2004. Q tomography of the upper mantle using three-component long-period waveforms. *Geophys. J. Int.* 157, 813–830.
- Helffrich, G., Asencio, E., Knapp, J., Owens, T., 2003. Transition zone structure in a tectonically inactive area: 410 and 660 km discontinuity properties under the northern North Sea. *Geophys. J. Int.* 155, 193–199.
- Hernandez, E., Alfe, D., Brodholt, J., 2013. The incorporation of water into lower-mantle perovskites: A first-principles study. *Earth Planet. Sci. Lett.* 364, 37–43.

- Huang, X., Xu, Y., Karato, S., 2005. Water content in the transition zone from electrical conductivity of wadsleyite and ringwoodite. *Nature* 434, 746–749.
- Iwamori, H., 2007. Transportation of H₂O beneath the Japan arcs and its implications for global water circulation. *Chem. Geol.* 239, 182–198.
- Jacobsen, S., van der Lee, S., 2006. Earth's deep water cycle. In: *Geophys. Monogr.*, vol. 168, pp. 1–313.
- Karato, S., 2003. Mapping water content in the upper mantle. In: *Geophysical Monograph: Inside the Subduction Factory*, pp. 135–152.
- Karato, S., 2011. Water distribution across the mantle transition zone and its implication for global material circulation. *Earth Planet. Sci. Lett.* 301, 413–423.
- Kelbert, A., Schultz, A., Egbert, G., 2009. Global electromagnetic induction constraints on transition-zone water content variations. *Nature* 460, 1003–1006.
- Kohlstedt, T., Keppler, H., Rubie, D., 1996. The solubility of water in α , β and γ phases of (Mg, Fe)₂SiO₄. *Contrib. Mineral. Petrol.* 123, 345–357.
- Komatitsch, D., Tromp, J., 1999. Introduction to the spectral-element method for 3-D seismic wave propagation. *Geophys. J. Int.* 139, 806–822.
- Kustowski, B., Ekström, G., Dziewonski, A., 2008a. Anisotropic shear-wave velocity structure of the Earth's mantle: A global model. *J. Geophys. Res.* 113, B06306, <http://dx.doi.org/10.1029/2007JB005169>.
- Kustowski, B., Ekström, G., Dziewonski, A., 2008b. The shear-wave velocity structure in the upper mantle beneath Eurasia. *Geophys. J. Int.* 174, 978–992.
- Lailly, P., 1983. The seismic inverse problem as a sequence of before stack migration. In: Bednar, J. (Ed.), *Conference on Inverse Scattering: Theory and Application*. Society for Industrial and Applied Mathematics, pp. 206–220.
- Laske, G., Masters, G., 1996. Constraints on global phase velocity maps from long-period polarization data. *J. Geophys. Res.* 101 (B7), 16,059–16,075.
- Lawrence, J., Wysession, M., 2006. Seismic evidence for subduction-transported water in the lower mantle. In: *Geophysical Monograph: Earth's Deep Water Cycle*, pp. 251–261.
- Liu, Q., Tromp, J., 2008. Finite-frequency sensitivity kernels for global seismic wave propagation based upon adjoint methods. *Geophys. J. Int.* 174, 265–286.
- Liu, H.P., Anderson, D.L., Kanamori, H., 1976. Velocity dispersion due to anelasticity: implications for seismology and mantle composition. *Geophys. J. R. Astron. Soc.* 47, 41–58.
- Maggi, A., Tape, C., Chen, M., Chao, D., Tromp, J., 2009. An automated time-window selection algorithm for seismic tomography. *Geophys. J. Int.* 178, 257–281.
- Maruyama, S., Okamoto, K., 2007. Water transportation from the subducting slab into the mantle transition zone. *Gondwana Res.* 11, 148–165.
- Meijde, M., Marone, F., Giardini, D., Lee, S., 2003. Seismic evidence for water deep in earth's upper mantle. *Science* 300, 1556–1558.
- Montagner, J.P., Anderson, D., 1989. Petrological constrains on seismic anisotropy. *Phys. Earth Planet. Inter.* 54, 82–105.
- Montelli, R., Nolet, G., Dahlén, F., Masters, G., Engdahl, E., Hung, S., 2004. Finite-frequency tomography reveals a variety of plumes in the mantle. *Science* 303, 338–343.
- Peter, D., Komatitsch, D., Luo, Y., Martin, R., Goff, L., Casarotti, E., Loher, L., Magnoni, P., Liu, Q., Blitz, C., Nissen-Meyer, T., Basini, P., Tromp, J., 2011. Forward and adjoint simulations of seismic wave propagation on fully unstructured hexahedral meshes. *Geophys. J. Int.* 186, 721–739.
- Piromallo, C., Morelli, A., 2003. P wave tomography of the mantle under the Alpine-Mediterranean area. *J. Geophys. Res.* 108, 2065, <http://dx.doi.org/10.1029/2002JB001757>.
- Romanowicz, B., 1995. A global tomographic model of shear attenuation in the upper mantle. *J. Geophys. Res.* 100, 12,375–12,394.
- Romanowicz, B., 2003. Global mantle tomography: Progress status in the past 10 years. *Annu. Rev. Earth Planet. Sci.* 31, 303–328.
- Ruan, Y., Zhou, Y., 2010. The effects of 3-D anelasticity (Q) structure on surface wave phase delays. *Geophys. J. Int.* 181, 479–492.
- Ruan, Y., Zhou, Y., 2012. The effects of 3-D anelasticity (Q) structure on surface wave amplitudes. *Geophys. J. Int.* 189, 967–983.
- Rychert, C., Fischer, K., Abers, G., Plank, T., Syracuse, E., Protti, J., Gonzalez, V., Strauch, W., 2008. Strong along-arc variations in attenuation in the mantle wedge beneath Costa Rica and Nicaragua. *Geochem. Geophys. Geosyst.* 9, <http://dx.doi.org/10.1029/2008GC002040>.
- Sacks, I., Okada, H., 1974. A comparison of the anelasticity structure beneath western south America and Japan. *Phys. Earth Planet. Inter.* 9, 211–219.
- Schiavardi, R., Morelli, A., 2011. Epmantle: a 3-D transversely isotropic model of the upper mantle under the European Plate. *Geophys. J. Int.* 185, 469–484.
- Shapiro, N., Ritzwoller, M., 2002. Monte Carlo inversion for a global shear velocity model of the crust and upper mantle. *Geophys. J. Int.* 151, 88–105.
- Shito, A., Karato, S., Matsukage, K., Nishihara, Y., 2006. Toward mapping water content, temperature and major element chemistry in Earth's upper mantle from seismic tomography. In: *Geophysical Monograph: Earth's Deep Water Cycle*, pp. 225–236.
- Simmons, N., Myers, S., Johannesson, G., Matzel, E., 2012. Llnl-g3dv3: Global P wave tomography model for improved regional and teleseismic travel time prediction. *J. Geophys. Res.* 117, <http://dx.doi.org/10.1029/2012JB009525>.
- Song, T., Helmberger, D., Grand, S., 2004. Low-velocity zone atop the 410-km seismic discontinuity in the northwestern United States. *Nature* 427, 530–533.
- Stachnik, J., Abers, G., Christensen, D., 2004. Seismic attenuation and mantle wedge temperature in the Alaska subduction zone. *J. Geophys. Res.* 109, B10304, <http://dx.doi.org/10.1029/2004JB003018>.
- Tape, C., Liu, Q., Tromp, J., 2007. Finite-frequency tomography using adjoint methods—Methodology and examples using membrane surface waves. *Geophys. J. Int.* 168, 1105–1129.
- Tape, C., Liu, Q., Maggi, A., Tromp, J., 2009. Adjoint tomography of the southern California crust. *Science* 325, 988–992.
- Tape, C., Liu, Q., Maggi, A., Tromp, J., 2010. Seismic tomography of the southern California crust based on spectral-element and adjoint methods. *Geophys. J. Int.* 180, 433–462.
- Tarantola, A., 1984. Inversion of seismic reflection data in the acoustic approximation. *Geophysics* 49, 1259–1266.
- Tauzin, B., Debayle, E., Wittlinger, G., 2010. Seismic evidence for a global low-velocity layer within the Earth's upper mantle. *Nat. Geosci.* 3, 718–721.
- Tromp, J., Tape, C., Liu, Q.Y., 2005. Seismic tomography, adjoint methods, time reversal and banana-doughnut kernels. *Geophys. J. Int.* 160, 195–216.
- Van der Hilst, R., Widjiantoro, S., Engdahl, E.R., 1997. Evidence for deep mantle circulation from global tomography. *Nature* 386, 578–584.
- Wiens, D., Conder, J., Faul, U., 2008. The seismic structure and dynamics of the mantle wedge. *Annu. Rev. Earth Planet. Sci.* 36, 421–455.
- Woodhouse, J., Dziewonski, A., 1984. Mapping the upper mantle: Three-dimensional modeling of Earth structure by inversion of seismic waveforms. *J. Geophys. Res.* 89, 5953–5986.
- Wortel, M.J.R., Spakman, W., 2000. Subduction and slab detachment in the Mediterranean-Carpathian region. *Science* 290, 1910–1917.
- Zhang, H., Thurber, C., Shelly, D., Ide, S., Beroza, G., Hasegawa, A., 2004. High-resolution subducting-slab structure beneath northern Honshu, Japan, revealed by double-difference tomography. *Geology* 32, 361–364.
- Zhao, D., Tian, Y., Lei, J., Liu, L., Zheng, S., 2009. Seismic image and origin of the Changbai intraplate volcano in East Asia: Role of big mantle wedge above the stagnant Pacific slab. *Phys. Earth Planet. Inter.* 173, 197–206.
- Zhou, Y., Dahmen, F., Nolet, G., 2004. Three-dimensional sensitivity kernels for surface wave observables. *Geophys. J. Int.* 158, 142–168.
- Zhu, H., Bozdog, E., Peter, D., Tromp, J., 2012. Structure of the European upper mantle revealed by adjoint tomography. *Nat. Geosci.* 5, 493–498.